Design and validation of a nanoscale cross-wire probe (X-NSTAP)

Matthew K. Fu[1] · **Yuyang Fan**[2] · **Marcus Hultmark**[1]

Abstract

A nano-sized crossed thermal anemometer (X-NSTAP) was developed and validated for measurements of two-components of velocity at high Reynolds numbers. The new sensor design is based on the single-component nanoscale thermal anemometry probe (NSTAP) previously used to acquire streamwise velocity measurements at high Reynolds numbers. The new sensor can, simultaneously, measure two components of velocity with a spatial resolution of $42 \times 42 \times 50\,\mu m$, an order of magnitude smaller in each dimension than conventional cross-wires. The new X-NSTAP design features several structural and manufacturing modifications to improve the aerodynamic performance of the sensor compared to previous nanoscale cross-wire designs. The effects of different manufacturing modifications were evaluated using dye visualizations over scale models of the sensor tip. The pitch sensitivity of the final sensor design was evaluated in an open-loop wind-tunnel and was comparable to the single-component NSTAP design. The X-NSTAP was then deployed in the Princeton Superpipe to acquire axial and radial velocity measurements up to friction Reynolds numbers, $Re_\tau = 24{,}000$ with good agreement to existing studies.

1 Introduction

In recent years, there have been significant advancements in our understanding of the behavior and scaling of turbulent fluctuations at high Reynolds numbers. The combination of specialized high Reynolds number facilities with new subminiature, fast-response instrumentation has revealed phenomena which have previously been hidden by sensor attenuation (Hutchins et al. 2009; Hultmark et al. 2012). Often, this attenuation stems from spatial filtering of the flow field when the sensing element exceeds the smallest scales in the flow and will be exacerbated at higher Reynolds numbers as the separation between the flow scales increases (Willmarth and Sharma 1984; Ligrani and Bradshaw 1987a, b; Smits et al. 2011). To address these limitations, a nanoscale thermal

anemometry probe (NSTAP) was developed at Princeton University that features a freestanding, $60 \times 2 \times 0.1\,\mu m$, platinum-sensing element, an order of magnitude smaller than conventional probes (see Fig. 1a). Fabrication of this new device was made possible with semiconductor and micro-electro-mechanical system (MEMS) manufacturing techniques that have been thoroughly described by Bailey et al. (2010), Vallikivi et al. (2011) and Vallikivi and Smits (2014).

The NSTAP is operated in the same manner as a conventional hot-wire and has been utilized in several high Reynolds number flow studies. The NSTAP has been deployed in several different facilities and flow configurations, with favorable results. It was first used in the Princeton Superpipe to study the scaling of streamwise velocity fluctuations in turbulent pipe flow at bulk Reynolds numbers up to $Re_D = 2U_b R/\nu = 6 \times 10^6$ (see Hultmark et al. 2012, 2013), where U_b is the bulk velocity, ν is the kinematic viscosity, and R is the pipe radius. There, the streamwise turbulence intensities were found to exhibit a logarithmic profile consistent with the theoretical predictions of Townsend (1976) and Perry et al. (1986), previously masked by probe resolution. Similarly, the NSTAP revealed clear logarithmic behavior in a zero-pressure gradient turbulent boundary layer by Vallikivi et al. (2015) as well as the continued log-linear growth of the inner peak (Samie et al. 2018). Furthermore, the NSTAP has also been used to reveal an unexpected

✉ Matthew K. Fu
mkfu@princeton.edu

Yuyang Fan
yuyang@tendo.tech

Marcus Hultmark
hultmark@princeton.edu

[1] Department of Mechanical and Aerospace Engineering, Princeton University, Engineering Quadrangle, Princeton, NJ 08544, USA

[2] Tendo Technologies, Inc., 303 College Road East, Suite A, Princeton, NJ 0850, USA

(a) Diagram of original NSTAP probe and scanning electron microscope image of the $60 \times 2 \times 0.1$ μm platinum sensing located at the probe tip

(b) Coordinate system for pitch (α) and yaw (β) angles for NSTAP and /-NSTAP experimentsa
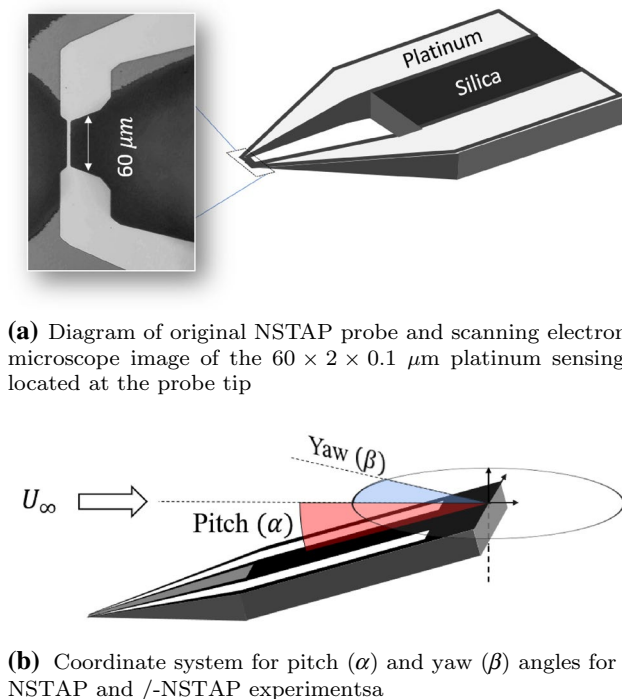
Fig. 1 Diagrams of conventional NSTAP design and coordinate system

influence of dissipative effects on the inertial-range statistics of classical grid turbulence at high Reynolds number (Sinhuber et al. 2017). Despite these advancements, the conventional NSTAPs are inherently limited to single-component measurements of turbulence, i.e., the streamwise component of velocity. Nevertheless, in wall-bounded turbulent flows, the wall-normal component of velocity is especially important, as it plays a key role in turbulent transport towards and away from the wall and contributes to the dominant Reynolds shear stress component, $\overline{u'v'}$.

Perhaps the most common tool for multi-component turbulence measurements is the cross-wire anemometer, composed of two hot-wires placed in close proximity but different orientations with respect to the incoming flow (e.g., an "X" configuration). Through appropriate calibration, the two components of velocity in the plane of the wires can be decomposed from both of the signals. A typical cross-wire probe has a sensing volume of approximately $1000 \times 1000 \times 1000$ μm, which is significantly larger than the smallest scales in most turbulent flow facilities, and more than two orders of magnitude larger than the smallest scales present in the Superpipe at high Reynolds numbers. Consequently, there have been numerous efforts to develop sub-miniature, MEMS versions of cross-wires, most of which have been met with mixed results. Attempts such as those made by Löfdahl et al. (1992) and Chen et al. (2003) either did not improve the spatial resolution of the sensor

or suffered from end-conduction effects. Vallikivi et al. (2012) developed and evaluated the performance of a single, inclined version of the NSTAP, dubbed the /-NSTAP. This NSTAP variant had a sensing wire with the same dimensions as the conventional NSTAP ($60 \times 2 \times 0.1$ μm), but oriented at a 45° angle to the incoming flow on an asymmetric probe body, allowing maximum sensitivity to both streamwise and wall-normal velocity components. The design was evaluated in turbulent pipe flow with encouraging, although very scattered, results. Fan et al. (2015) presented a novel method for combining two /-NSTAPs to form a nano-scale cross-wire version of the NSTAP probe, dubbed the X-NSTAP. While the resulting probe was found to exhibit excellent yaw sensitivity with constant cooling angles from $-15°$ to $15°$, the bulky and asymmetric probe design resulted in an adverse sensitivity to pitch angle (α), making the sensor unsuitable for most turbulence measurements (see Fig. 1b).

Here, the development of a significantly improved X-NSTAP design capable of two-component velocity measurements at high Reynolds numbers is described. The new sensor design was informed by dye visualization in a laminar water channel over scale models of different NSTAP and /-NSTAP geometries to reveal the influence of the support structure on the flow field. Significant blockage was found over the /-NSTAP design considered by Fan et al. (2015) and Vallikivi et al. (2012), explaining the undesired sensitivity to pitch angles. After iterating through different support structure configurations to determine an adequate geometry, it was found that the /-NSTAP design needed to be re-engineered with considerably thinner support structures to avoid interference with the sensing element. Despite the original /-NSTAP support tip being 10 μm thick at the leading edge, the flow visualization revealed that a tip thickness of $\sim$ 1 μm was necessary to mitigate flow obstruction. This was achieved by removing the silicon features in the proximity of the sensing element and replacing it with a significantly less bulky support. To ensure the structural integrity of the thinner, metallic features at the probe tip, a 1.4 μm thick layer of amorphous tungsten was added, significantly improving the robustness with a negligible change to the blockage. The resulting tip was found to have significantly less sensitivity to pitch angle, with performance comparable to the original NSTAP design. Using the novel combining method developed by Fan et al. (2015), a sub-miniature cross-wire could then be fabricated with a sensing volume of $42 \times 42 \times 50$ μm, an order of magnitude smaller in each dimension than conventional cross-wire probes. Because the dimensions of the wire filaments are identical to that of the single-component NSTAP, the probe has a significantly improved frequency response compared with conventional hot-wires due to the minuscule thermal mass of the sensing elements. The performance of the combined probe was
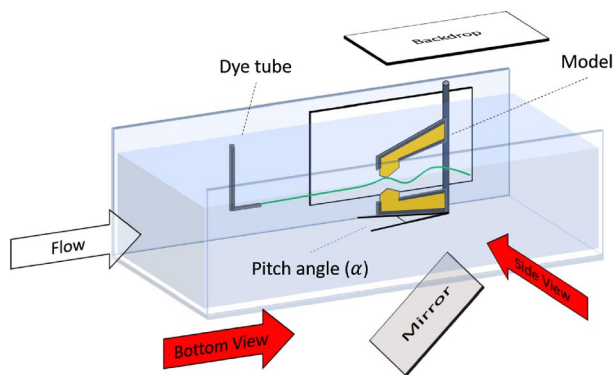
(a) Flow visualization water channel diagram
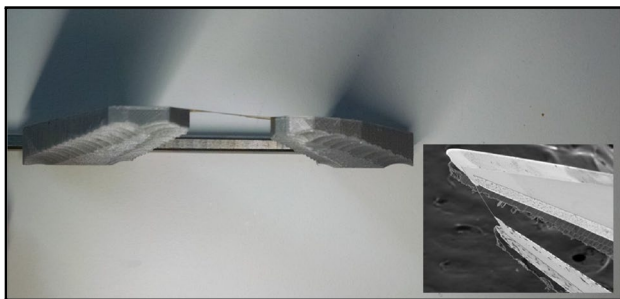
(b) Scale model of /-NSTAP tip.

Fig. 2 Flow visualization setup for the /-NSTAP. **a** Diagram of NSTAP model mounted in the water channel (flow direction is from left to right) with two cameras capturing side and bottom views of the flow interaction. The red arrows indicate the direction of the cameras. **b** Image of the assembled 3D-printed model with the mock polyimide sensing element; inset is a SEM image of an actual probe, showing good resemblance to the between the scale model and actual sensor

then evaluated in the Princeton Superpipe with a convincing agreement to existing high Reynolds number measurements.

2 Redesigning the /-NSTAP

2.1 Flow visualization of the probe tip

To better understand the flow obstruction created by the probes and improve their design, 3D-printed models of the regular and inclined NSTAPs (/-NSTAP) were tested in a low-speed water channel with a 3 m long test section and a 0.45×0.3 m cross-section. Two cameras were positioned to capture side and bottom views of the flow interaction (see Fig. 2a). 250:1 scale models of the NSTAP and /-NSTAP tips were fabricated with a laser-cut polyimide sheet (15 mm $\times$ 500 µm $\times$ 25 µm) in place of the platinum-sensing element and a 3D-printed support structure (fused deposition modeling of polylactic acid filament) in place of the silicon. To nominally match the model's Reynolds number with those encountered by the actual

sensor in a typical wind tunnel experiment, the water tunnel was operated at its minimum speed where the flow was observed to be steady, approximately 15 mm s^{-1}. This corresponds to a Reynolds number based on the wire width of $Re_b = U_\infty b \nu^{-1} = 7.5$, where b is the 500 µm width of the model wire, and U_∞ is the freestream velocity of the channel. Due to the limited channel cross-sectional area, the models were limited to 125 mm in length, corresponding to the leading 500 µm from the tip of the actual probes. Figure 2b shows a head-on view one of the models with a scanning electron microscope (SEM) image of an actual probe tip.

Green food dye was diluted to a density slightly higher than that of water and used to visualize the flow around the models. The dye reservoir was set at the level of the channel-free surface, and dye was dispensed at approximately the same velocity of the flow. Images and videos of the visualization were captured for dye released at a few different locations at pitch angles of 0° and 8°.

Three different models of the probe tips were considered. First, the symmetric, single-component NSTAP model was considered as a baseline. Next, the original /-NSTAP design from Fan et al. (2015) was then evaluated to investigate the effects of the asymmetry on the flow field. Finally, a modified version of the /-NSTAP model was fabricated to emulate a tip with significantly thinner silicon support structures, and a sensing element shifted upstream. Representative visualizations of the flow around the tips of the NSTAP and Fan et al. (2015) /-NSTAP can be seen in the left and right columns of Fig. 3, corresponding to flow at 0° and 8° pitch angles, respectively. Streaklines of the green dye qualitatively show the interactions between the flow and the model. Figure 3a, b shows the symmetric NSTAP model at the two different pitch angles. In both cases, the streaklines appear unaffected by the pitch angles at the wire.

In the case of the original /-NSTAP model used by Fan et al. (2015) (see Fig. 3c, d), clear obstruction from the longer, asymmetric, "silicon support" is observed as significant changes in the streaklines. This effect is more easily seen from the bottom views of the same model in Fig. 3e, f. While the longer support does not seem to alter the flow very much at 0° pitch angle (see Fig. 3e), when the model is pitched, disturbance to the flow creates 3-dimensional structures as seen in both Fig. 3d, f. These results are consistent with the characterization made by Fan et al. (2015), who proposed that the sensitivity to pitch angle was due to the silicon support structure near the wires, especially the frontmost one. Finally, in an attempt to mitigate these pitch-angle effects, a modified /-NSTAP model with thinner support structures, exposing more of the polyimide film, and upstream-positioned sensing element was evaluated. Figure 3g, h shows how the new /-NSTAP model with reduced support thickness generates less disturbance to the flow compared to the original
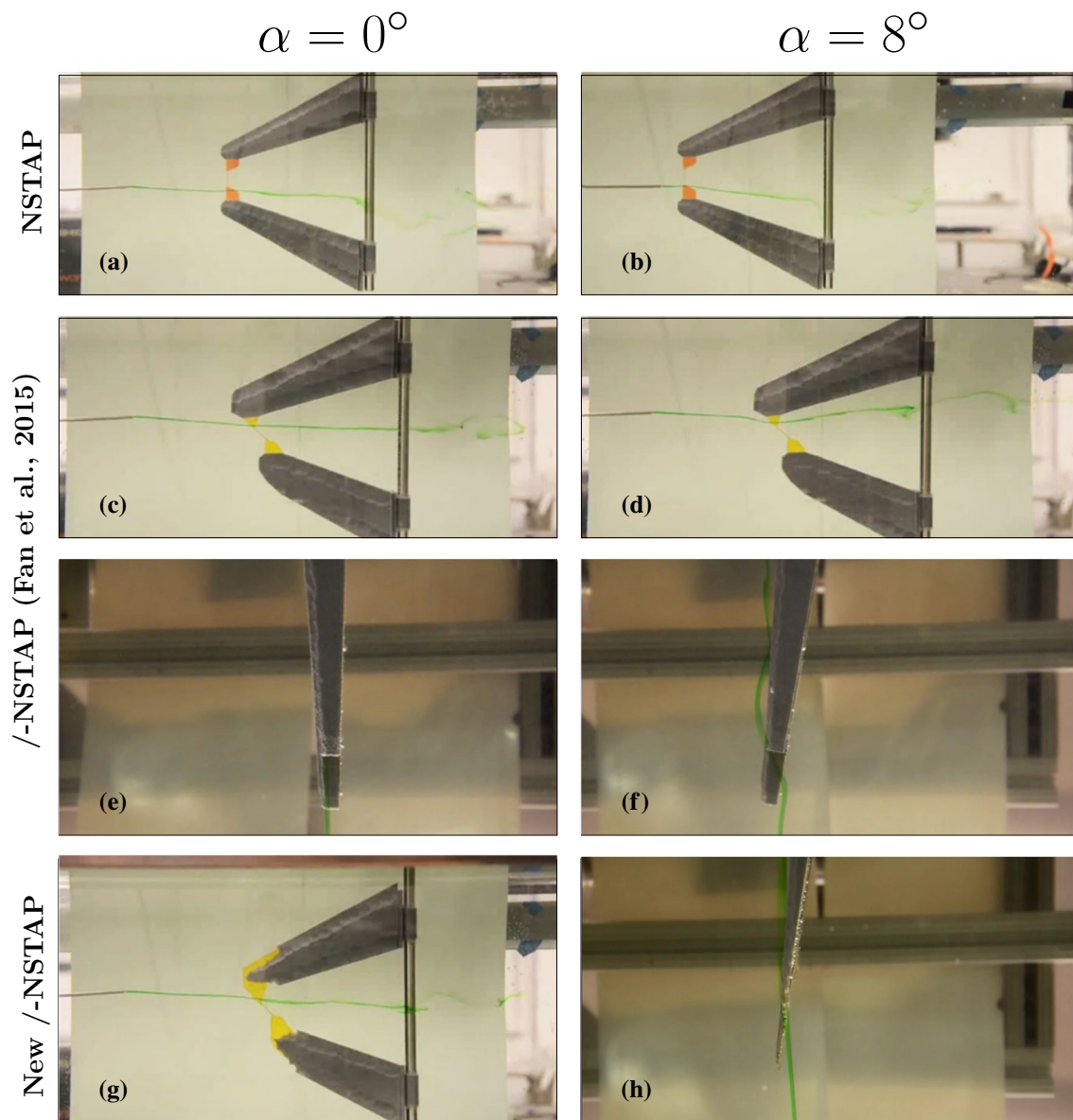
$$\alpha = 0°$$ $$\alpha = 8°$$

Fig. 3 Dye visualization of NSTAP and /-NSTAP models of Fan et al. (2015) at 250:1 scale. Silicon supports are replaced by grey 3D-printed models and the metallic features with a polyimide film. **a**, **c**, **e**, **g** Models at 0° pitch angle, **b**, **d**, **f**, **h** are models at 8° pitch angle. **a**, **b** The model of the symmetric, single-component NSTAP, without much flow disturbance near the wire at the pitched configuration; **c**, **d** show the model of the original /-NSTAP, and flow is obstructed when the model is pitched; **e**, **f** are bottom views of the same /-NSTAP from **c**, **d** (flow goes upward). A clean streakline with 0° pitch angle can be seen, but clear disturbance when the model is pitched. **g**, **h** The model of a thinner, redesigned /-NSTAP (less support material). The side views of the old /-NSTAP (**c**) and new /-NSTAP (**g**) at $\alpha = 0°$ show similar streakline behavior. However, the bottom view (**h**) of the new /-NSTAP shows significantly less disruption at $\alpha = 8°$ compared to **f**

/-NSTAP design, further substantiating the hypothesis of Fan et al. (2015). This is most evident in the bottom view shown in Fig. 3h where the streakline is significantly less affected by the new probe body compared to the original /-NSTAP design in Fig. 3f.

2.2 Tungsten-tipped sensors

While reducing the size of the silicon supports is necessary to improve the aerodynamic performance of the probe, this new design would significantly compromise the robustness of the structures at the tip. In particular, reducing the amount of silicon exposes more of the 100 nm-thick platinum stubs and prongs, creating a larger, more fragile, freestanding structure compared

to the original /-NSTAP. Therefore, to reinforce the platinum stubs/prongs, a relatively thick layer of amorphous tungsten ($\sim 1.4\,\mu\mathrm{m}$) is sputtered onto the platinum side, covering the stubs and prongs (not the sensing wire) before backside deep reactive ion etching (DRIE) takes place to release individual sensors. Tungsten was chosen because it has a relatively large Young's modulus among pure metals and can be processed using sputtering deposition, allowing it to be layered at a precise thickness on top of the metal features to increase their stiffness without significantly increasing the blockage. An additional 60 nm of platinum was added to the top of the tungsten layer to protect it from reacting in the plasma environment, which considerably improved the quality and consistency of the probes. Importantly, any residual stress from thin film deposition will try to release itself once the rigid substrate is removed. This effect will cause the thin films to curl once the excess silicon is removed. Great care was taken to achieve an amorphous metallic film free of stresses by adjusting the argon deposition pressure in the magnetron sputtering system (Shen et al. 1999). While the most relevant alterations and additions to the /-NSTAP fabrication have been detailed above, a complete recipe for fabricating the thin /-NSTAP probes is detailed in Fan (2017).

2.3 Pitch angle sensitivity

To evaluate the pitch angle (α) sensitivity of the new /-NSTAP design, velocity measurements were obtained in an open loop wind tunnel capable of free stream velocities from 5–20 m s^{-1}. The probe was mounted onto a manual rotary traverse to vary the probe pitch angle with respect to the incoming flow field and operated with a Dantec Dynamics StreamLine® Constant Temperature Anemometer circuit. Here, pitch sensitivities were evaluated at a free stream velocity of $U_\infty = 14$ m s^{-1} that was measured via a Pitot-static tube. A comparison of the pitch sensitivities between the symmetric NSTAP, original /-NSTAP, and the modified /-NSTAP designs can be seen in Fig. 4. Velocity measurements for each probe are normalized by the "true" velocity measured at $\alpha = 0$ and their deviation at different pitch angles is plotted. Though the sensing element dimensions for symmetric NSTAP and /-NSTAP are the same, the /-NSTAP has the sensing element at 45° to the incoming flow at $\alpha = 0$. Results (in black) for the symmetric NSTAP and original /-NSTAP are adapted from Fan et al. (2015). The symmetric NSTAP design exhibits changes of less than 2% for pitch angles $-15° \leq \alpha \leq 15°$, while the original /-NSTAP design exhibits deviations up to 20% from the "true" velocity for the same range. Importantly, the new /-NSTAP design exhibits a significantly reduced sensitivity to pitch angle compared to the original /-NSTAP and is even slightly better than the symmetric NSTAP design at larger α.
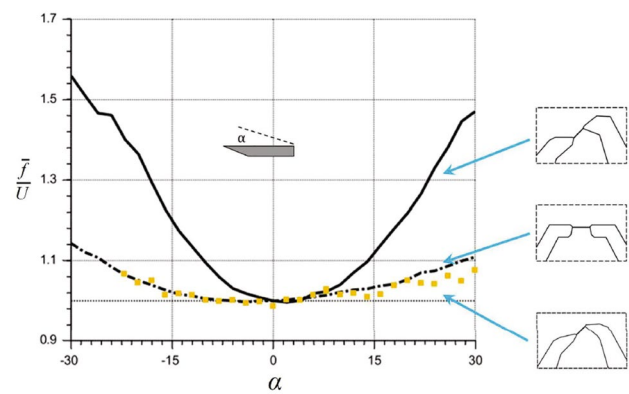

Fig. 4 Velocity measurement sensitivity to pitch angle (α) for different probe designs. Mean velocity measurements, $\bar{f}$, for the different probe designs are shown at different pitch angles, α, normalized by the "true" velocity measured evaluate at $\alpha = 0$, U. (Dashed lines): pitch angle sensitivity of the conventional, straight-wire NSTAP design. Deviations from the "true" velocity measured at $\alpha = 0$ are below 1% for $|\alpha| \leq 10°$ Vallikivi and Smits (2014). (Solid lines): pitch angle sensitivity of the inclined single-wire NSTAP angled at 45° developed by Fan et al. (2015). Deviations from the "true" velocity measured at $\alpha = 0$ are significant for all pitch angles considered. (Yellow filled square box): pitch angle sensitivity of a newly designed inclined single-wire NSTAP angled at 45°. Deviations from the "true" velocity measured at $\alpha = 0$ are comparable to the conventional NSTAP design and demonstrate a significant improvement over the Fan et al. (2015) design. All measurements were taken at free stream velocity of $U_\infty = 14$ m s^{-1}. Note that the inclined NSTAP has the sensing element at 45° to the incoming flow at $\alpha = 0$. Image adapted from Fan et al. (2015)

3 Combining probes to make a nanoscale cross-wire probe (X-NSTAP)

The /-NSTAPs that compose the X-NSTAP have an asymmetric configuration with sensing wires positioned at a 45° angle to the incoming flow. To form a set of crossed wires within a small volume, it is crucial to keep the two sensing wires in close proximity without any physical or electrical contact.

A precise gap between the two probes is achieved with the novel probe combination technique outlined by Fan et al. (2015) (see Fig. 5a). The two NSTAPs are attached with their flat sides facing each other with a polyimide film used as the spacer. DuPont™Kapton® polyimide is flexible, mechanically robust, chemically inert, electrically insulating, thermally stable, and can be made as thin as 25 µm. The X-NSTAPs in this study are fabricated with an ultrasmooth, 50 µm thick Kapton film that was patterned with gold traces (250 nm thick with a 10 nm adhesion layer). These gold traces were patterned on both sides of the Kapton film, allowing each probe to be electrically connected to the stainless steel prongs and the operating circuit (see Fig. 5b). A flip chip bonder (Research Devices) and conductive silver epoxy (EPO-TEK® H22) were used to combine
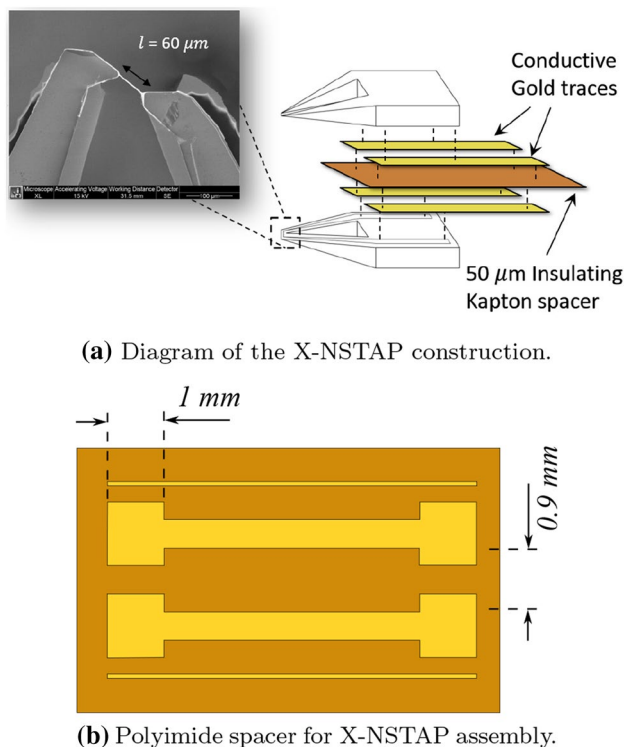
(a) Diagram of the X-NSTAP construction.

(b) Polyimide spacer for X-NSTAP assembly.

Fig. 5 Illustration of the probe combination technique introduced by Fan et al. (2015). **a** Two /-NSTAPs are assembled with their flat faces (i.e., the side that contains the sensing element and electrical traces) facing each other. The traces on the sensors are attached to the gold traces with conductive silver epoxy. **b** Illustration of the polyimide spacer used in the X-NSTAP assembly. The thickness of the spacer sets the separation of the sensing elements. Gold traces are patterned symmetrically on both sides of the film to allow for electrical connections to the sensing element

the /-NSTAP, Kapton, and prong assembly. Images of the X-NSTAP probe tip at different viewing angles can be seen in Fig. 6. Figure 6a shows the two /-NSTAP probes sandwiching the polyimide spacer from the side, while Fig. 6c more clearly shows the resulting 50 μm gap between the two /-NSTAPs. Figure 6b, d shows the probe tip from the size and illustrate the extent of the freestanding metal structures and the "X" formed by the sensing elements. The resulting measurement volume formed by the two probes is $42 \times 42 \times 50$ μm.

4 Experimental methodology

4.1 Princeton Superpipe facility

To evaluate the performance of the newly designed probe, measurements were conducted in the Princeton Superpipe, a fully turbulent pipe flow facility that utilizes compressed air up to 220 atm as the working fluid.

The details of the pipe facility are outlined extensively by Zagarola and Smits (1998), but the most relevant parameters are reiterated here. Tests were conducted in a smooth pipe of radius, $R = 64.68$ mm which can achieve Reynolds numbers between $3.1 \times 10^4 < Re_D < 3.5 \times 10^7$. The surface finish on the pipe is estimated to have a root mean square roughness of $k_{rms} = 0.15 \pm 0.03$ μm and is shown to be hydraulically smooth up to $Re_D = 13.5 \times 10^6$ $(Re_\tau = Ru_\tau v^{-1} < 217 \times 10^3)$ in McKeon et al. (2004), which exceeds the Reynolds numbers investigated in this study. The streamwise pressure drop and the friction velocity, u_τ, were calculated using twenty 0.8 mm diameter static wall pressure taps spaced evenly at 165.1 mm streamwise increments upstream of the test section, where u_τ is determined from the wall shear stress, τ_w, and fluid density, ρ, as $u_\tau = \sqrt{\tau_w \rho^{-1}}$. The measurement station is located approximately 196 diameters from the pipe entrance, and a measurement traverse is used to span the radius of the pipe. The differential pressure between the static taps was measured with a 1333 Pa range MKS transducer. The temperature of the working fluid was monitored with a K-type thermocouple and found to vary no more than ± 0.1 °C during a test.

4.2 Instrumentation

The X-NSTAP was operated using a Dantec Dynamics StreamLine® Constant Temperature Anemometer circuit with dual channels. Each wire of the X-NSTAP was operated at a nominal overheat ratio, $R_w/R_0 \approx 1.2$, where R_w is the resistance of the wire during operation and R_0 is the 'cold' resistance of the wire at ambient tunnel temperature. This overheat ratio roughly corresponds to a wire temperature of approximately 100 °C above the ambient temperature. A Pitot tube with an inner diameter of 0.89 m was used to calibrate the velocity sensitivity of the X-NSTAPs in situ. Static pressure was measured using two 0.40 mm static pressure taps located in the pipe wall at the same streamwise location as the tip of the Pitot tube. The differential pressure between the Pitot and static ports was measured with Validyne DP15 transducers with 1379 Pa, 8618 Pa, and 34,473 Pa ranges, and was used to calculate the local velocity at the location of the Pitot tube. These measurements were corrected for viscous effects associated with the size of the Pitot tube diameter in the manner outlined by McKeon et al. (2003) while turbulence and velocity gradients corrections outlined in the same study were found to have a negligible effect at the centerline. Similarly, the static pressure measurements used to calculate the dynamic pressure of the Pitot tube were corrected according to McKeon and Smits (2002) and were also found to have a negligible effect. The static gauge pressure of the working fluid was measured with an Omega PX303 transducer with a 500 psig range which, along with
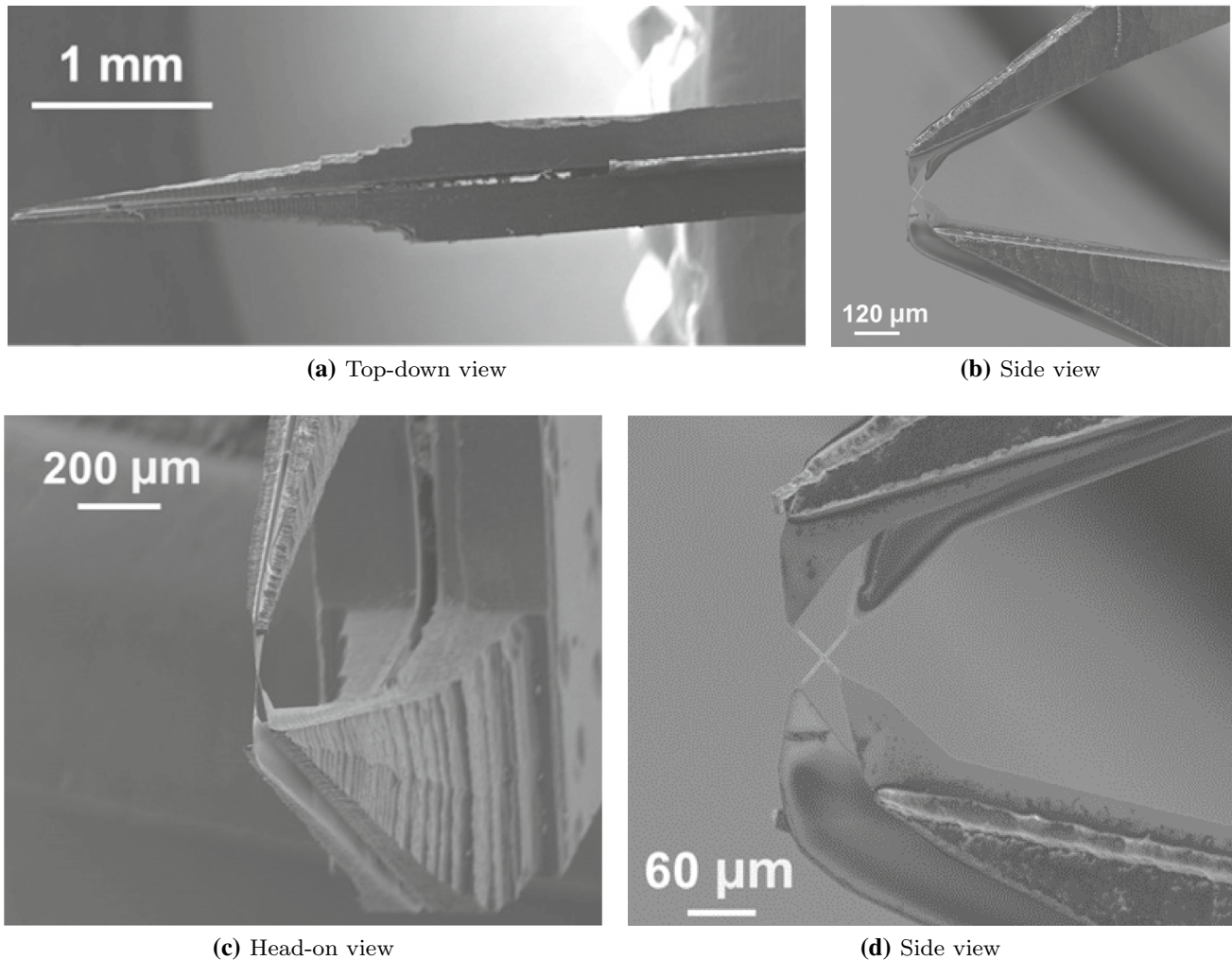
(a) Top-down view

(b) Side view

(c) Head-on view

(d) Side view

Fig. 6 Scanning electron microscope images of the crossed Nano Scale Thermal Anemometry Probe (X-NSTAP). **a** Top-down view of the X-NSTAP showing the two slanted NSTAP probes sandwiched with a Kapton spacer to separate the wires. **b** Side view of the X-NSTAP probe showing the arrangement of the sensing elements. **c** Head-on view of the X-NSTAP showing the sensing elements and the gap between the probes. **d** Close-up view of the crossed sensing elements

the tunnel temperature, was used to determine the properties of the working fluid, i.e., density and viscosity following the methodology outlined by Zagarola (1996).

The displacement of the nearest wall-normal position of the X-NSTAP sensing wires and Pitot tube was determined with a depth microscope (Titan Tool Supply Inc.) with positioning accuracy of ± 1 µm before obtaining measurements. A linear optical encoder (SENC50 Acu-Rite Inc.) was then used to track the wall normal displacement, and an electrical limit switch was used to ensure repeatable positioning near the wall. The X-NSTAP was oriented to simultaneously resolve axial (u_z) and radial (u_r) velocity components, such that the "X" formed by the wire was perpendicular to the wall. Due to the width of the X-NSTAP body, the closest the sensing element of the probe could be positioned in this configuration relative to the wall was approximately 1.5 mm.

The frequency response of the X-NSTAP wires was always found to exceed 150 kHz in still air from a square wave test. Data for each wire of the probe were sampled simultaneously at 300 kHz (National Instruments PCI-6123) and filtered at 150 kHz using an analog 8-pole Butterworth filter (Krohn-Hite Corporation), both of which exceeded the maximum flow frequencies encountered in this study.

4.3 Experimental parameters and calibration

The X-NSTAP was evaluated at friction Reynolds numbers, $Re_\tau = 1800$–24,000. A summary of the different test conditions can be found in Table 1. For all conditions considered in this study, the wire length, l, was less than 23 viscous length scales, or equivalently $l^+ \equiv l u_\tau \nu^{-1} < 23$, where the

Table 1 Experimental parameters for X-NSTAP measurements of turbulent pipe flow at high Reynolds numbers

Re_τ	P_{abs} (bar)	U_b (m·s^{-1})	νu_τ^{-1} (μm)	u_τ (m·s^{-1})	l/η_{min}	lu_τ/ν^{-1}	Line
1850	1.01	8.6	35.0	0.43	0.66	1.7	▪
3400	1.01	17.2	19.0	0.80	1.1	3.2	▪
12400	13.2	5.4	5.25	0.22	3	11.4	▪
20000	13.2	9.0	3.25	0.35	4.4	18.4	▪
24700	13.2	11.4	2.63	0.44	5.2	22.8	▪

P_{abs} is the absolute pressure in the facility

+ superscript is used in the conventional manner to denote normalization with inner parameters (i.e., u_τ and ν).

To calibrate the probe to the streamwise velocity, the Pitot tube and X-NSTAP probes were positioned symmetrically about the pipe centerline and calibration curves were populated using at least 18 different velocities spanning the range of expected velocities in each experiment. Calibration cycles were conducted before and after the experiments, and the resulting data were fit with a fourth-order polynomial. The directional sensitivity (i.e., cooling angles) of the individual X-NSTAP sensing wires was determined in situ using the "stress-calibration" method developed by Zhao et al. (2004). This method uses measurements of the streamwise pressure-gradient with the theoretical linearity of the total stress in fully developed pipe flow to determine the effective cooling angles of cross-wire probes. Calibration of the cooling angles for both probes occurs during the course of the measurement and statistics acquired over the pipe radius are fit to the theoretical stress curve.

Total stress distributions measured by the X-NSTAPs for the different test conditions can be seen in Fig. 7. The higher Reynolds number results ($Re_\tau > 10,000$) demonstrate reasonable agreement between the theoretical stress distribution and X-NSTAP stress measurements. However, there is a more noticeable discrepancy between the measured and expected stress distributions in the low Reynolds number measurements (e.g., $Re_\tau = 1850$), particularly in the near-wall region. These deviations most likely correspond to thermal interactions between the different sensing wires associated with the low Péclet number effects stemming from the close wire proximities. The Péclet number set by the wire separation, d, characteristic velocity, U, and fluid the thermal diffusivity, α_t, is given by $Pe_d = Ud \cdot \alpha_t^{-1}$; for the lowest Reynolds number measurements ($Re_\tau = 1850$), $Pe_d \approx 17$ near the wall and reaches $Pe_d \approx 30$ near the pipe centerline. However, Österlund and Johansson (1995) found that one should ensure $Pe_d > 50$ to eliminate thermal interactions between the wires, with significant correlations between the wires occurring for $Pe_d < 10$. Due to the nature of the signal decomposition associated with the effective cooling angle assumptions and "stress-calibration" method, thermal interactions between the wires will negligibly affect the streamwise velocity measurements but can influence measurements

of the wall-normal velocity component (see Appendix A for the details of the "stress-calibration" method). To determine which measurements were likely susceptible to these low Pe_d effects, each combination of radial locations and test conditions was evaluated against the $Pe_d < 50$ criteria recommended by Österlund and Johansson (1995). Based on this criteria, thermal interactions between the probes were found to be relevant only in the lowest Reynolds number case considered here ($Re_\tau = 1850$ for all radial locations, r) and the region close to the wall ($r > 0.8\,R$) for the $Re_\tau = 3400$ case. All other data sets were found to have $Pe_d > 50$ at all measurement locations and are unlikely to suffer from low Pe_d effects. In particular, this notion is evident in the highest Reynolds number cases ($Re_\tau > 10,000$), which exhibit a higher degree of linearity in the total stress throughout the pipe radius compared to the low Re_τ cases, see Fig. 7. For clarity, measurements involving wall-normal velocity that do not satisfy the Pe_d criterion have been rendered with smaller, faded markers and are only present in the lowest Re_τ cases.

To further ensure that these low Pe_d effects were avoided, the data considered here are fit to data in the central region of the pipe flow (where classical "outer" scaling dominates) corresponding to $r < 0.6\,R$ where the stress curve is linear and found to be relatively insensitive to choices of a cutoff for smaller choices of r as a cutoff. In this experiment, this criteria correspond to 11 points being used for the nonlinear regression and a coefficient of determination greater than 0.998 was found in all cases. For all the Reynolds numbers considered here, the viscous contribution to the total stress in this region was found to be insignificant.

5 Results

To quantify the probe performance, the time-averaged statistics (denoted by an overline) are compared with results from the existing literature, in particular, the mean and variances of the radial (u_r) and axial (u_z) velocity field. A summary of the selected data sets can be found in Table 2 with the most notable results coming from recent measurements in the Princeton Superpipe (Hultmark et al. 2012; Zhao and Smits 2007) and Center for International Cooperation in Long Pipe Experiments (CICLoPE) (Örlü et al. 2017;

Table 2 Reference studies and measurements of turbulent pipe flow at high Reynolds numbers

	Reference	Re_τ	l^+	Line
Princeton Superpipe	Hultmark et al. (2012) NSTAP - u'_z	1.8×10^3	1.8	
		3.3×10^3	3.1	
		5.4×10^3	5.0	
		10.5×10^3	9.7	
		20.2×10^3	18.8	
		37.5×10^3	17.4	
		68.3×10^3	31.7	
		98.1×10^3	45.5	
	Zhao and Smits (2007) Cross-wire - u'_z, u'_r	2.7×10^3	20.8	.....
		3.3×10^3	25.5	.....
		5×10^3	38.7	.....
		10×10^3	77	.....
		20×10^3	154	.....
		75×10^3	580	.....
		100×10^3	773	.....
CICLoPE	Örlü et al. (2017) Cross-wire - u'_z, u'_r	6.6×10^3	10.2	•—•
		14.6×10^3	22.8	•—•
		22.8×10^3	35.5	•—•
		31.2×10^3	48.6	•—•
		38.1×10^3	59.2	•—•
	Willert et al. (2017) PIV - u'_z, u'_r	20×10^3	32.2(z) 3.0(r) 13.6(θ)	- - -
DNS	Ahn et al. (2013)	180	-	══
		544	-	══
		934	-	══
	Ahn et al. (2015)	3008	-	══
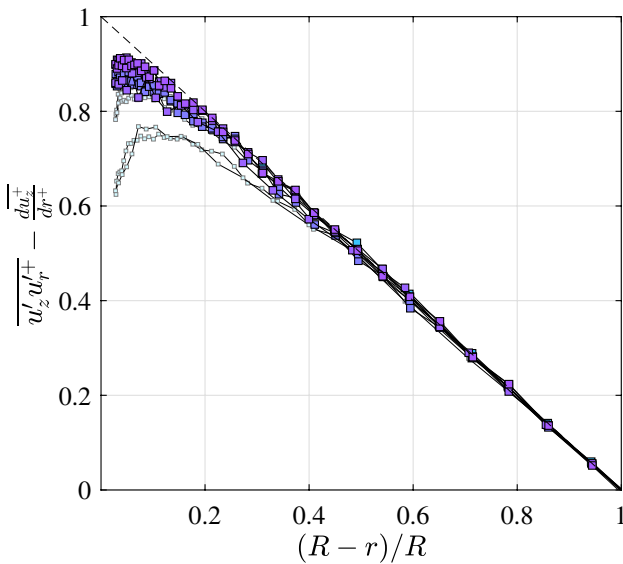
Fig. 8 Mean velocity profiles. (Purple filled square box): X-NSTAP measurements. (Purple solid lines): NSTAP measurements of Hultmark et al. (2011)

Willert et al. 2017). The current study is most similar to that of Örlü et al. (2017) with respect to instrumentation, spatial resolution, and Reynolds number range. However, the admitted uncertainty in friction velocity measured in CICLoPE by Örlü et al. (2017) limits the conclusive comparison between their cross-wire measurements and those from this study, warranting further investigation. Figure 8 shows excellent agreement between the mean velocity profiles ($\overline{u_z^+}$) measured with X-NSTAP in the Superpipe with measurements taken with conventional, single-component NSTAP measurements taken by Hultmark et al. (2012). Good agreement can also be found with available particle image velocimetry (PIV) profiles from CICLoPE taken by Willert et al. (2017), though not with the cross-wire measurements of Örlü et al. (2017).

The agreement between the radial profiles of the axial velocity variances ($\overline{u_z'^2}$) can be seen in Fig. 9, where ′ denotes the fluctuating component of the signal about the mean value, $\overline{u_z}$. When expressed in inner units, see Fig. 9a, some small deviations between the different data sets can be seen. At the lower Reynolds numbers, the X-NSTAP and NSTAP measurements demonstrate excellent agreement; though at the higher Reynolds numbers, the X-NSTAP measurements are a few percent larger than the NSTAP measurements in the logarithmic region with similar agreement to the cross-wire measurements of Örlü et al. (2017). However, when the radial profiles are normalized by the pipe radius, see Fig. 9b, there is a good agreement between all of the data sets. Due to the nature of the calibration associated with the effective cooling angle, low Pe_d effects likely present in

Fig. 7 Total stress distribution determined by the "stress-calibration" method of Zhao et al. (2004). ($\overline{u_z' u_r'}^+ - \frac{d\overline{u_z^+}}{dr^+}$) profiles. Smaller, faded square symbols denote measurements for $Re_\tau = 1850$ and $Re_\tau = 3400$ cases where $Pe_d < 50$, indicating likely thermal interactions between the individual wires based on the criteria of Österlund and Johansson (1995)
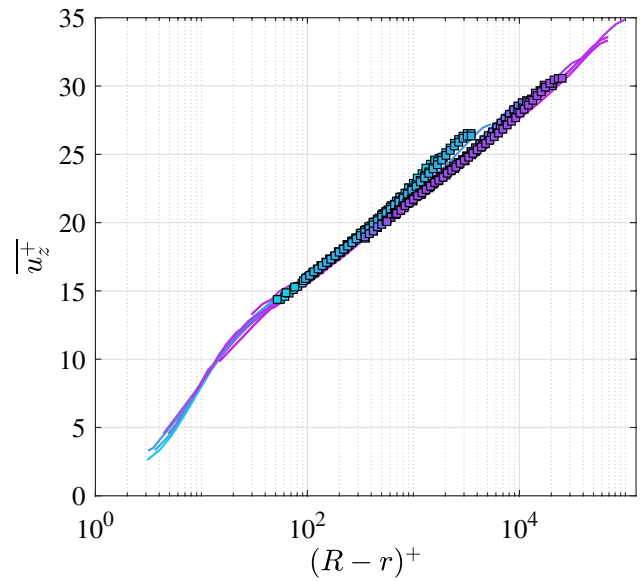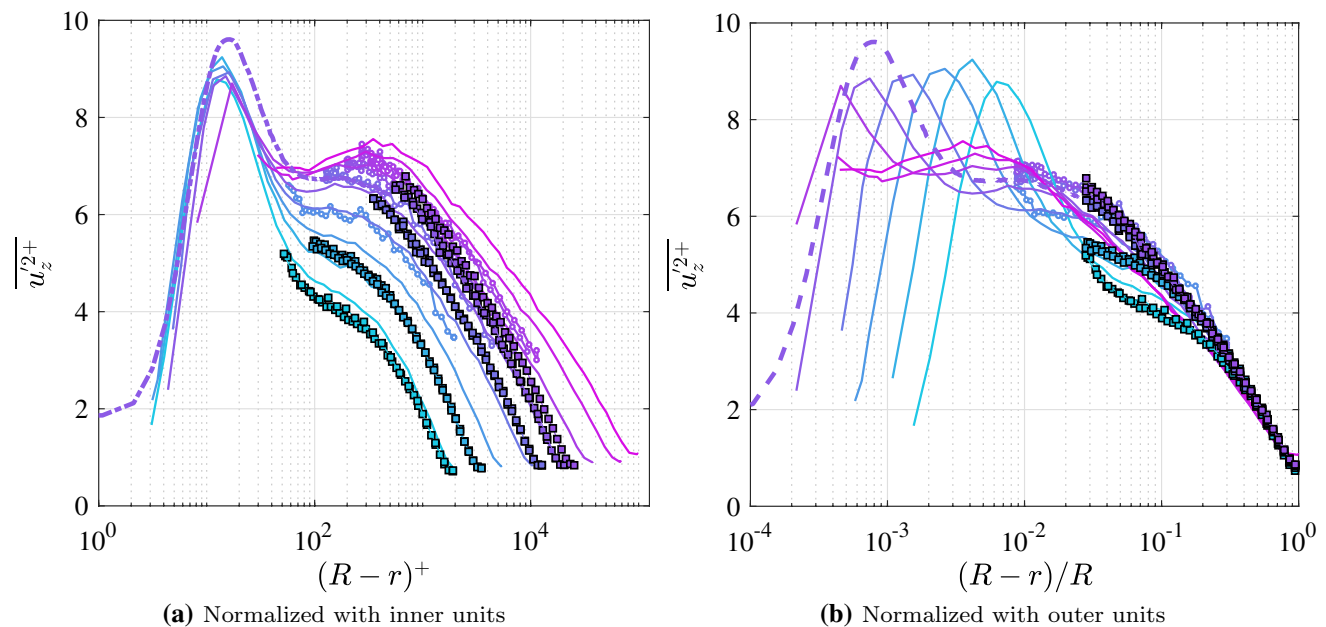
(a) Normalized with inner units

(b) Normalized with outer units

Fig. 9 Axial velocity variance ($\overline{u_z'^2}^+$) as a function of $[R-r]^+$ (**a**) and $[R-r]/R$ (**b**). (Purple square box): X-NSTAP measurements. (Purple

solid lines): NSTAP measurements of Hultmark et al. (2011). (Purple dashed lines): PIV measurements of Willert et al. (2017). (Purple circle): cross-wire measurements of Örlü et al. (2017)

the low Re_τ cases do not affect the mean or variance of the streamwise velocity.

The radial profiles of the radial velocity variances ($\overline{u_r'^2}$) can be seen in Fig. 10. When expressed in inner units, see Fig. 10a, it is clear that the X-NSTAP measurements at low Reynolds number exhibit a different profile shape compared to the DNS curves, especially closer to the wall. Where the DNS finds maxima in the wall-normal variance profile around $(R-r)^+ \approx 10^2$, the X-NSTAPs predict maxima further our near $(R-r)^+ \approx 10^3$. This behavior is likely an artifact of the thermal interaction between the different wires. When the wires are able to heat each other, the different wire signals will become correlated. Because of the nature of the angular calibration, the thermal interaction between the wires will manifest itself by decreasing the apparent measurement of u_r. The high Reynolds number results are incredibly encouraging demonstrating excellent agreement with the PIV results at $Re_\tau = 20,000$ (Willert et al. 2017). This agreement is most evident in Fig. 10b where one can see how $\overline{u_r'^2}$ measurements from the X-NSTAP meetup almost exactly with the PIV results. There is also surprising agreement between the higher Reynolds number measurements ($Re_\tau > 10,000$) and the earlier cross-wire measurements of Zhao and Smits (2007), who utilized a 500 µm cross-wire in the Princeton Superpipe. For $Re_\tau > 10,000$, the maximum of the X-NSTAP radial variance measurements occurs around $r = 0.1R$ and is approximately constant for $r < 0.1R$ at $\overline{u_r'^2}^+ \approx 1.3$–1.4. Interestingly, where the larger cross-wire results exhibit a noticeable increase in the wall-normal

variance as the probe approaches the pipe wall (Örlü et al. 2017; Zhao and Smits 2007), the X-NSTAP instead measures a very slight decrease in the variance towards the wall, similar to the measurements of Baidya et al. (2017) who used a conventional cross-wire in a high Reynolds number boundary layer.

6 Conclusions

A new nano-scale crossed hot-wire (X-NSTAP) has been designed, fabricated, and validated. The pitch angle sensitivity of the /-NSTAP design proposed by Fan et al. (2015) was examined with dye visualization and found to be an artifact of the asymmetric silicon supports. With the help of the dye visualization setup, a new probe design with slimmer silicon supports was created with significantly less effect on the flow when pitched. To ensure the structural robustness without increasing the form factor of the slimmer design, a 1.4 µm-thick layer of amorphous tungsten was layered onto the tip of the support structure. The pitch-angle sensitivity of the new probe design was then evaluated in a wind tunnel and found to be on par with that of the conventional NSTAP design, having less than 2% deviation for $|\alpha| \leq 15°$. Two of the new /-NSTAP probes were then combined with a 50 µm spacer and technique proposed by Fan et al. (2015) to create a newly redesigned X-NSTAP probe with a $42 \times 42 \times 50$ µm measurement volume.

(a) Normalized with inner units

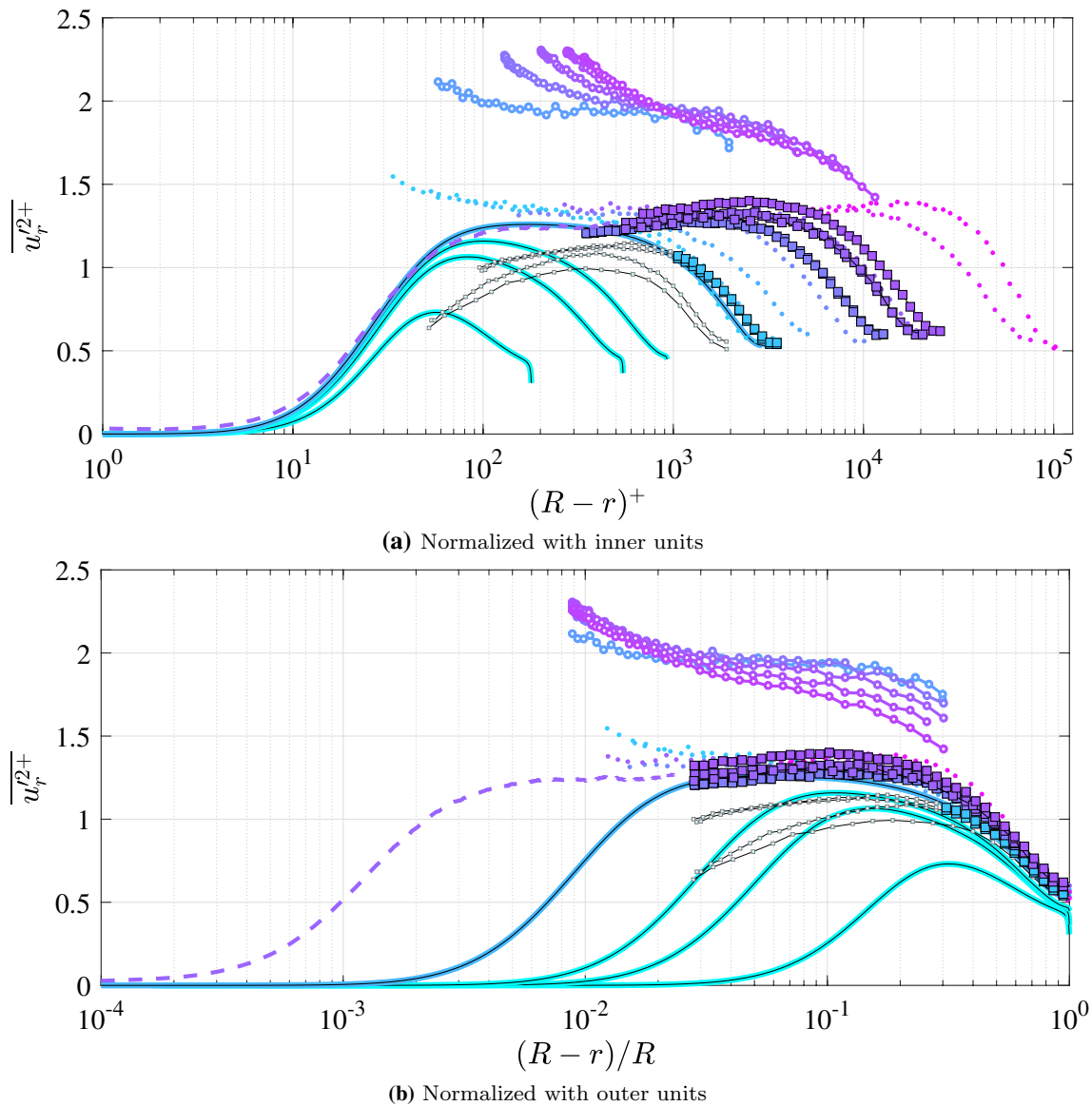**(b)** Normalized with outer units

Fig. 10 Wall-normal velocity variance ($\overline{u_r'^{2+}}$) as a function of $(R-r)^+$ (upper plot) and $(R-r)/R$ (bottom plot). (Purple square box): X-NSTAP measurements. (Purple dashed lines): PIV measurements of Willert et al. (2017). (Purple open circle): cross-wire measurements of Örlü et al. (2017). (Purple filled circle): cross-wire meas-urements of Zhao and Smits (2007). (Lines in skyblue): DNS results of Ahn et al. (2015) and Ahn et al. (2013). Smaller, faded square symbols denote measurements for $Re_\tau = 1850$ and $Re_\tau = 3400$ cases where $Pe_d < 50$, indicating likely thermal interactions between the individual wires based on the criteria of Österlund and Johansson (1995)

The probe was deployed in the Princeton Superpipe to acquire radial and axial velocity measurements up to $Re_\tau = 24,000$. Axial velocity measurements (mean and variance) taken with the X-NSTAP demonstrate good agreement with the single-component NSTAP measurements of Hultmark et al. (2012). Due to the close proximity of the two sensing wires, radial measurements near the wall at low Reynolds numbers suffer from low Péclet number effects where the two wires can thermally interact. Consequently, the low Reynolds number results from the X-NSTAP

measurements exhibit a different profile shape and overall lower magnitude near the wall compared with DNS results. This behavior is consistent with the findings of Österlund and Johansson (1995), but further work is needed to characterize these thermal interactions.

Measurements of the radial velocity variance at higher Reynolds numbers ($Re_\tau = 20,000$) demonstrate excellent agreement with the PIV results from CICLoPE of Willert et al. (2017) and are found to plateau around $\overline{u_r'^{2+}} \approx 1.3$ at $r < 0.1R$, see Fig. 10. This value, however, is lower than the

comparable measurements from Örlü et al. (2017) acquired with a conventional cross-wire probe in CICLoPE which plateaus at $\overline{u_r'^{2+}} \approx 1.8$. In contrast to both of those results, there is a small but observable increase in the peak magnitude of $\overline{u_r'^{2+}}$ from $\overline{u_r'^{2+}} \approx 1.32$ in the $Re_\tau = 20{,}000$ case to $\overline{u_r'^{2+}} \approx 1.4$ $Re_\tau = 24{,}700$ case. While the current results are promising, more results, particularly at higher Reynolds numbers, are needed to explore the theoretical predictions of Perry et al. (1986) and Townsend (1976). Despite the improvements to the aerodynamic design of the /-NSTAP probe, structural robustness remains one of, if not the primary, limitation to the successful application of these probes. Further work is necessary to improve the yield of structurally robust probes, particularly for measurements in compressed air facilities such as the Princeton Superpipe where the aerodynamic forces are significantly augmented by the increased fluid density.

Appendix A: "Stress-Calibration" method of Zhao et al. (2004)

In this study, the "stress-calibration" method of Zhao et al. (2004) was to calibrate the angle sensitivity of the two X-NSTAP wires, the major details of which are reproduced below. For a hot-wire inclined with respect to the incoming flow, the "effective" cooling velocity, u_e, as determined from the hot-wire output voltage is assumed to be geometrically related to the instantaneous velocity components by an effective cooling angle, ϕ, by the cosine law of cooling (see Bradshaw 1971).

In a fully developed pipe flow where $\overline{u_r} = 0$, the instantaneous velocities in the coordinate system of the pipe can be geometrically related to the effective cooling velocity by

$$u_{e1} = \overline{u_z}\cos\phi_1 + u_z'\cos\phi_1 + u_r'\sin\phi_1, \qquad (1)$$

$$u_{e2} = \overline{u_z}\cos\phi_2 + u_z'\cos\phi_2 - u_r'\sin\phi_2, \qquad (2)$$

where subscripts 1 and 2 denote the cooling velocities and angles for the two different wires in the probe, overlines denote the time-averaged quantity, and ′ denotes the fluctuating component about the mean value. If one assumes that the local turbulence is spatio-temporally resolved by each wire and the cooling angles are independent of Reynolds number, then Eqs. (1) and (2) can be expressed as

$$u_{e1}\cos^{-1}\phi_1 = \overline{u_z} + u_z' + u_r'\tan\phi_1 = f(E_1, \phi_1), \qquad (3)$$

$$u_{e2}\cos^{-1}\phi_2 = \overline{u_z} + u_z' - u_r'\tan\phi_2 = g(E_2, \phi_2), \qquad (4)$$

where f and g functions that relate the anemometer output voltage, E, for the different wires to the effective cooling velocity. Since ϕ is assumed to be a constant for each wire, the calibration functions can be represented as fourth-order polynomials (Bruun (1995)) given by

$$f(E_1) = \sum_{i=0}^{4} a_i E_1^i, \qquad (5)$$

$$g(E_2) = \sum_{i=0}^{4} b_i E_2^i, \qquad (6)$$

where the explicit dependence of f and g on ϕ_1 and ϕ_2 into absorbed into the calibration constants, a_i and b_i. Time averaging Eqs. (5) and (6) yields

$$\overline{f} = \overline{u_z} = \sum_{i=0}^{4} a_i \overline{E_1^i}, \qquad (7)$$

$$\overline{g} = \overline{u_z} = \sum_{i=0}^{4} b_i \overline{E_2^i}, \qquad (8)$$

which relates the mean anemometer output to the mean streamwise velocity. Using Eqs. (7) and (8), the calibration coefficients can be determined by varying the mean velocity, U_z, and anemometer output, E. Here, calibration was by placing the hot-wire probe and a Pitot tube symmetrically about the pipe centerline where the mean velocity gradient is negligible and turbulence intensity is low and varying the tunnel speed.

While the streamwise sensitivity of the individual wires has been established, one still needs to determine the cooling angles, ϕ_1 and ϕ_2, to fully relate the anemometer outputs to the instantaneous velocity components. Here, we will use the known distribution of the total stress, τ_T, in fully-developed, incompressible, turbulent pipe flow to determine, ϕ_1 and ϕ_2. For a smooth pipe, the total stress distribution is given by

$$\frac{\tau_T}{\rho} = u_\tau^2 = \overline{u_z u_r} - \nu\frac{dU_z}{dr} = -\frac{1}{2\rho}\frac{dP}{dz}(r), \qquad (9)$$

where dP/dz is the streamwise pressure-gradient. Considering the fluctuation components of Eqs. (3) and (4) gives

$$u_z' + u_r'\tan\phi_1 = f - \overline{f} = f',$$
$$u_z' - u_r'\tan\phi_2 = g - \overline{g} = g',$$

which can be expressed as

$$u'_z + \zeta u'_r = \frac{1}{2}(f' + g'), \tag{10}$$

$$\xi u'_r = \frac{1}{2}(f' - g'), \tag{11}$$

where

$$\zeta = \frac{1}{2}(\tan\phi_1 - \tan\phi_2), \tag{12}$$

$$\xi = \frac{1}{2}(\tan\phi_1 + \tan\phi_2). \tag{13}$$

Multiplying both Eqs. (10) and (11) by (11) and averaging gives

$$\xi\overline{u'_z u'_r} + \zeta\xi\overline{u'^2_r} = \frac{1}{4}(\overline{f'^2} - \overline{g'^2}), \tag{14}$$

$$\xi^2\overline{u'^2_r} = \frac{1}{4}\overline{(f' - g')^2}. \tag{15}$$

Through simple rearranging, Eq. (10) can be substituted into Eq. (11) giving

$$\xi^2\overline{u'_z u'_r} = \frac{\xi}{4}(\overline{f'^2} - \overline{g'^2}) - \frac{\zeta}{4}(\overline{f'^2} - \overline{g'^2}). \tag{16}$$

To determine ζ and χ, one simply gathers and computes the fluctuating statistics corresponding to $\overline{f'^2}$, $\overline{g'^2}$, and $\overline{f'^2} - \overline{g'^2}$ at different radial locations in the pipe where the viscous stress contribution is negligible. Conveniently this can be accomplished during the course of a typical experimental measurement, making angular calibration and data acquisition one and the same. Since the Reynolds shear stress component can be determined from the pressure-gradient and radial location in this region, the only unknowns left in Eq. (16) are ζ and χ. Substituting the measurements from the different radial locations into Eq. (16) and conducting a nonlinear curve fit allows us to determine the error minimizing values for ζ and χ and by extension, ϕ_1 and ϕ_2. Once the cooling angles are known, the fluctuating velocity components, u'_z and u'_r, can be related to the f' and g' through

$$u'_z = \frac{f' + g'}{2} - \frac{\zeta(f' - g')}{2\xi}, \tag{17}$$

$$u'_r = \frac{(f' - g')}{2\xi}. \tag{18}$$

If the wires suffer from low Péclet number effects, the individual wire signals will be correlated to each other as one wire heats the other, and vice versa. Compared to the radial velocity measurements, the thermal correlation is not expected to significantly influence the axial velocity measurements. Since the probe is calibrated using varying streamwise velocities, the thermal correlation between the wires is explicitly accounted for in the mean velocity measurements. From Eq. (18), one can see that the radial measurements will be strongly impacted by the thermal correlation between the wires as the difference between the wire signals will be materially diminished. However, Eq. (17) shows that the fluctuating component of the axial velocity is computed using both the sum and difference between the two fluctuating wire signals, f' and g', the former of which is larger in magnitude and proportionally less affected by this consideration.

References

Ahn J, Lee JH, Jang SJ, Sung HJ (2013) Direct numerical simulations of fully developed turbulent pipe flows for Re τ = 180, 544 and 934. Int J Heat Fluid Flow 44:222–228

Ahn J, Lee JH, Lee J, Kang Jh, Sung HJ (2015) Direct numerical simulation of a 30R long turbulent pipe flow at Re τ = 3008. Phys Fluids 27(6):065110

Baidya R, Philip J, Hutchins N, Monty JP, Marusic I (2017) Distance-from-the-wall scaling of turbulent motions in wall-bounded flows. Phys Fluids 10(1063/1):4974354

Bailey SCC, Kunkel GJ, Hultmark M, Vallikivi M, Hill JP, Meyer KA, Tsay C, Arnold CB, Smits AJ (2010) Turbulence measurements using a nanoscale thermal anemometry probe. J Fluid Mech 663:160–179. https://doi.org/10.1017/S0022112010003447

Bradshaw P (1971) An introduction to turbulence and its measurement. Pergamon Press, Oxford, New York, pp 106–133

Bruun HH (1995) Hot-wire anemometry: principles and signal analysis. Oxford University Press, pp 89–158. ISBN: 0198563426, 9780198563426

Chen J, Fan Z, Zou J, Engel J, Liu C (2003) Two-dimensional micromachined flow sensor array for fluid mechanics studies. J Aerosp Eng 16(2):85–97

Fan Y (2017) High resolution instrumentation for flow measurements. Ph.D. thesis, Princeton University

Fan Y, Arwatz G, Van Buren TW, Hoffman DE, Hultmark M (2015) Nanoscale sensing devices for turbulence measurements. Exp Fluids 56(7):138

Hultmark M, Ashok A, Smits AJ (2011) A new criterion for end-conduction effects in hot-wire anemometry. Meas Sci Technol 22(5):055401

Hultmark M, Vallikivi M, Bailey SCC, Smits AJ (2013) Logarithmic scaling of turbulence in smooth- and rough-wall pipe flow. Journal of Fluid Mechanics 728:376–395

Hultmark MN, Vallikivi M, Bailey SCC, Smits AJ (2012) Turbulent pipe flow at extreme Reynolds numbers. Phys Rev Lett 108(9):1–5

Hutchins N, Nickels T, Marusic I, Chong MS (2009) Hot-wire spatial resolution issues in wall-bounded turbulence. J Fluid Mech 635:103–136

Ligrani PM, Bradshaw P (1987a) Spatial resolution and measurement of turbulence in the viscous sublayer using subminiature hot-wire probes. Exp Fluids 5(6):407–417

Ligrani PM, Bradshaw P (1987b) Subminiature hot-wire sensors: development and use. J Phys E Sci Instrum 20(3):323–332

Löfdahl L, Stemme G, Johansson B (1992) Silicon based flow sensors used for mean velocity and turbulence measurements. Exp Fluids 12(4):270–276. https://doi.org/10.1007/BF00187305

McKeon BJ, Smits AJ (2002) Static pressure correction in high Reynolds number fully developed turbulent pipe flow. Meas Sci Technol 13:1608–1614. https://doi.org/10.1088/0957-0233/13/10/314

McKeon BJ, Li J, Jiang W, Morrison JF, Smits AJ (2003) Pitot probe corrections in fully developed turbulent pipe flow. Meas Sci Technol 14(8):1449–1458

McKeon BJ, Swanson CJ, Zagarola MV, Donnelly RJ, Smits AJ (2004) Friction factors for smooth pipe flow. J Fluid Mech 511:41–44

Örlü R, Fiorini T, Segalini A, Bellani G, Talamelli A, Alfredsson PH (2017) Reynolds stress scaling in pipe flow turbulence first results from CICLoPE. Philo Trans R Soc Lond A Math Phys Eng Sci 375(2089):20160187

Österlund JM, Johansson AV (1995) Dynamic behavior of hot-wire probes in turbulent boundary layers. In: Benzi R (ed) Advances in turbulence V. fluid mechanics and its applications, vol 24. Springer, Dordrecht

Perry AE, Henbest S, Chong MS (1986) A theoretical and experimental study of wall turbulence. J Fluid Mech 165:163–199

Samie M, Marusic I, Hutchins N, Fu MK, Fan Y, Hultmark M, Smits AJ (2018) Fully resolved measurements of turbulent boundary layer flows up to Re τ = 20000. J Fluid Mech 851:391–415

Shen YG, Mai YW, Zhang QC, McKenzie DR, McFall WD, McBride WE (1999) Residual stress, microstructure, and structure of tungsten thin films deposited by magnetron sputtering. J Appl Phys 87(1):177. https://doi.org/10.1063/1.371841

Sinhuber M, Bewley GP, Bodenschatz E (2017) Dissipative effects on inertial-range statistics at high reynolds numbers. Phys Rev Lett 119:134502. https://doi.org/10.1103/PhysRevLett.119.134502

Smits AJ, Monty JP, Hultmark M, Bailey SCC, Hutchins N, Marusic I (2011) Spatial resolution correction for wall-bounded turbulence measurements. J Fluid Mech 676(2011):41–53. https://doi.org/10.1017/jfm.2011.19

Townsend AA (1976) The structure of turbulent shear flow. Cambridge University Press, Cambridge, New York

Vallikivi M, Smits AJ (2014) Fabrication and characterization of a novel nanoscale thermal anemometry probe. J Microelectromech Syst 23(4):899–907. https://doi.org/10.1109/JMEMS.2014.2299276

Vallikivi M, Hultmark M, Bailey SCC, Smits AJ (2011) Turbulence measurements in pipe flow using a nano-scale thermal anemometry probe. Exp Fluids 51(6):1521–1527

Vallikivi M, Hultmark M, Smits AJ (2012) Turbulence measurements at high Reynolds numbers using a new inclined nano-scale thermal anemometry probe. In: 18th Australasian fluid mechanics conference, Launceston, Australia, 3–7 Dec 2012

Vallikivi M, Ganapathisubramani B, Smits AJ (2015) Spectral scaling in boundary layers and pipes at very high Reynolds numbers. J Fluid Mech 771:303–326

Willert CE, Soria J, Stanislas M, Klinner J, Amili O, Eisfelder M, Cuvier C, Bellani G, Fiorini T, Talamelli A (2017) Near-wall statistics of a turbulent pipe flow at shear Reynolds numbers up to 40000. J Fluid Mech 826:R5

Willmarth WW, Sharma LK (1984) Study of turbulent structure with hot wires smaller than the viscous length. J Fluid Mech 142:121

Zagarola MV (1996) Mean-flow scaling of turbulent pipe flow. Ph. D. thesis, Princeton University

Zagarola MV, Smits AJ (1998) Mean-flow scaling of turbulent pipe flow. J Fluid Mech 373:S0022112098002419

Zhao R, Smits AJ (2007) Scaling of the wall-normal turbulence component in high-Reynolds-number pipe flow. J Fluid Mech 576:457–473

Zhao R, Li J, Smits A (2004) A new calibration method for crossed hot wires. Meas Sci Technol 15(9):1926–1931